



Impact of North Brazil Current rings on air-sea CO₂ flux variability in winter 2020

Léa Olivier¹, Jacqueline Boutin¹, Gilles Reverdin¹, Nathalie Lefèvre¹, Peter Landschützer², Sabrina Speich³, Johannes Karstensen⁴, Markus Ritschel² and Rik Wanninkhof⁵

5 ¹ LOCEAN-IPSL, Sorbonne Université-CNRS-IRD-MNHN, Paris, France

² Max Planck Institute for Meteorology, Hamburg, Germany

³ Laboratoire de Météorologie Dynamique, ENS-Ecole Polytechnique-CNRS-Sorbonne Université, Paris, France

⁴ GEOMAR Helmholtz Centre for Ocean Research, Kiel, Germany

⁵ Atlantic Oceanographic & Meteorological Laboratory of NOAA, Miami, USA

10

Correspondence to: Léa Olivier (lea.olivier@locean.ipsl.fr)

Abstract. The North Brazil Current (NBC) flows northward across the Equator, passes the mouth of the Amazon River, and forms large oceanic eddies near 8°N. We investigate the processes driving the variability of air-sea CO₂ fluxes at different
15 scales in early 2020 in the region [50°W-59°W – 5°N-16°N]. This region is a pathway between the equatorial and North Atlantic Ocean and was surveyed during the EUREC⁴A-OA/ATOMIC campaign. In-situ surface fugacity of CO₂ (fCO₂), salinity and temperature combined with maps of satellite salinity, chlorophyll-a and temperature highlight contrasting properties in the region. In February 2020, the area is a CO₂ sink (-1.7 TgC.month⁻¹), previously underestimated by a factor
20 10. The NBC rings transport saline and high fCO₂ water indicative of their equatorial origins and are a small source of CO₂ at regional scale. Their main impact on the variability of biogeochemical parameters is through the filaments they entrain into the open ocean. During the campaign, a nutrient rich freshwater plume from the Amazon River is entrained from the shelf up to 12°N and caused a phytoplankton bloom leading to a significant carbon drawdown (~20 % of the total sink). On the other hand, saltier filaments of shelf water rich in detrital material act as strong local sources of CO₂. Spatial distribution of fCO₂ is therefore strongly influenced by ocean dynamics south of 12°N. The less variable North Atlantic subtropical water extends
25 from Barbados northward. They represent ~60 % of the total sink due to their lower temperature associated with winter cooling and strong winds.

1 Introduction

The North Brazil Current is one of the dominant features of the tropical Atlantic circulation. In a region dominated by zonal
30 jets, it flows northward along the coast of South America and separates from the coast around 6-8°N. It seasonally retroflects to feed the North Equatorial Counter Current and thus close the equatorial wind-driven gyre. This retroflexion occasionally



pinches off some of the world's largest eddies, the North Brazil Current rings (NBC rings, Johns et al., 1990; Richardson et al., 1994).

35 After their separation from the NBC retroflection region, the rings travel north-westward toward the Caribbean in a course parallel to the coast of South America. These eddies have been extensively studied using modelling and both, in-situ (e.g. 1998-2001 NBC Ring experiment, Wilson et al., 2002) and satellite observations. They have a mean radius of 200 km and their diameter can exceed 450 km. Vertically, some of them extend down to more than 1000 m (Fratantoni & Glickson, 2002; Fratantoni & Richardson, 2006; Johns et al., 2003). Different family of rings exists, and most of the anticyclonic eddies

40 detectable by altimetry are rather shallow, extending from the surface to 200-300 m (Garraffo et al., 2003; Wilson et al., 2002). They swirl clockwise and travel with an average north-westward translation speed of 8-15 km d⁻¹ (Johns et al., 1990; Mélice & Arnault, 2017). When they reach the Lesser Antilles, they start to coalesce and disintegrate, partly due to interactions with the topography (Fratantoni & Richardson, 2006; Jochumsen et al., 2010). There is substantial variability in the number of rings shed per year, ranging from 5 (Aroucha et al., 2020; Fratantoni & Glickson, 2002; Mélice & Arnault, 2017, Goni & Johns,

45 2001) to 9 (Johns et al., 2003). NBC rings play a crucial role in the interhemispheric transport of salt and heat in the Atlantic Ocean and are an important part of the meridional overturning circulation (Johns et al., 2003). The NBC rings disrupt an already complex region located in the vicinity of the Amazon River mouth and at the transition between equatorial and subtropical waters.

50 While most of the studies on rings focused on their physical properties, little is known about their biogeochemical properties and how they affect the air-sea CO₂ flux of the western tropical Atlantic. The global ocean acts as an atmospheric CO₂ sink, taking up 23% of total anthropogenic CO₂ emissions (Friedlingstein et al., 2020) and causing ocean acidification (IPCC, 2019; 2021). The equatorial Atlantic Ocean is the second-largest source of CO₂ to the atmosphere after the equatorial Pacific (Landschützer et al., 2014; Takahashi et al., 2009). The concentration of atmospheric CO₂ is continuously increasing due to

55 human activities (IPCC, 2019; 2021), and characterizing the role of the ocean in mitigating climate change through CO₂ uptake is thus a key investigation. Previous works in this region examined the influence of the equatorial upwelling and of the Amazon plume on the CO₂ flux. CO₂-rich equatorial waters, originating from the equatorial upwelling (Andrié et al., 1986) strongly contrast with the CO₂ undersaturated Amazon River plume waters. The magnitude of the Amazon River discharge is unique in the global ocean. It represents as much freshwater as the next 7 largest rivers in the world combined and contributes to

60 almost 20% of global river freshwater input to the ocean (Dai & Trenberth, 2002). It therefore strongly impacts the physical, biogeochemical and biological properties of the coastal and the open ocean. Often overlooked, the Amazon River plume is an atmospheric CO₂ sink of global importance (Ibáñez et al., 2016). The plume carries water rich in silicate, nitrogen and phosphate into the tropical oceanic waters that are strongly depleted in nutrients. As water mixes and turbidity decreases, the primary producer's growth and associated biological drawdown are stimulated (Chen et al., 2012). Nitrogen is rapidly

65 consumed, and nitrogen fixation by diazotrophs becomes the main pathway of carbon sequestration in the plume



(Subramaniam et al., 2008). This strong carbon drawdown leads to a significant sink of atmospheric CO₂ (Körtzinger, 2003; Lefèvre et al., 2010). Not taking into account the Amazon plume would result in overestimating the tropical Atlantic air-sea CO₂ flux by 10% (Ibáñez et al., 2016).

70 The Amazon River's discharge reaches a minimum in December and progressively increases from January onwards. The plume extension is minimum in that season (Fournier et al., 2015) and as a result, it is the season of maximum salinity in the northwestern tropical Atlantic. The difference between the fugacity of CO₂ (fCO₂) in the surface ocean and in the atmosphere (ΔfCO₂) climatology over 1998-2015 divides the north-western tropical Atlantic into two regions (Figure 1a). The Amazon outflow region is particularly hard to reconstruct due to its strong variability and a severe lack of data. Waters located in the
75 southeasternmost part of the domain act as a strong source of CO₂ to the atmosphere. The source progressively transitions into a sink north of 10°N as waters get colder linked to the seasonal winter cooling. This situation is typical of a transition zone between equatorial and subtropical waters in winter (Landschützer et al., 2020, Figure 1a). The freshwater of the Amazon remains mainly confined to the continental shelf due to winds perpendicular to the coast as they travel northwestward into the Caribbean Sea (Coles et al., 2013). However, it has recently been documented that off-shore freshwater transport is often
80 present in February and significantly alters the physical properties of the region (Reverdin et al., 2021). This is partly due to the interaction of the NBC rings with the Amazon plume (Figure 1c). The ocean color signature of the Amazon (Muller-Karger et al., 1988) has been used as a tracer to delineate the rings, and better understand their generation, evolution and characteristics (Johns et al., 1990; Fratantoni & Glickson, 2002). For example, Figure 1b shows two filaments stirred by two large rings. The Amazon River also influences the surface temperature and salinity of the rings. They are considered warm-core rings but have
85 a warm SST anomaly in the first half of the year, and a cold one in the second half, because the anomaly is relative to the regional SST, with an extensive warm pool in late summer and autumn (Ffield, 2005). Their signature in salinity is therefore plume-dependent as well. Ffield (2005) reported that 3 out of 4 rings were surrounded by lower salinity water. This is also highlighted in February 2020 where an NBC ring stirs a plume of fresher water rich in chlorophyll-a toward the open ocean (Figure 1b,c). Salinity and chlorophyll-a are therefore critical to understand the surface physical and biogeochemical properties
90 of the region, as well as the air-sea fluxes of CO₂ (Figure 1).

The northwestern tropical Atlantic is a dynamically active region, containing eddies several hundred kilometers in diameter and connected to the world's largest river. There are surprisingly few biogeochemical observations available for winter months during low outflow from the Amazon River. Few tropical Atlantic measurements of biogeochemical tracers are available with
95 one transect in winter in the Surface Ocean CO₂ Atlas (SOCAT, Bakker et al., 2016) database south of 10°N crossing the region. This scarcity is a major impediment in understanding the biological and physical processes underlying the oceanic carbon and nutrient cycles in the region. Satellite surface chlorophyll-a and salinity show a strong spatial structure, with eddies, filaments, and a fresh water plume (Figure 1 b,c). In this study, we take advantage of the physical and biogeochemical data



collected during the EUREC⁴A-OA/ATOMIC experiment in January-February 2020, combined with satellite data, to
100 understand how the NBC rings and their related structures impact the air-sea fluxes of CO₂ in winter.

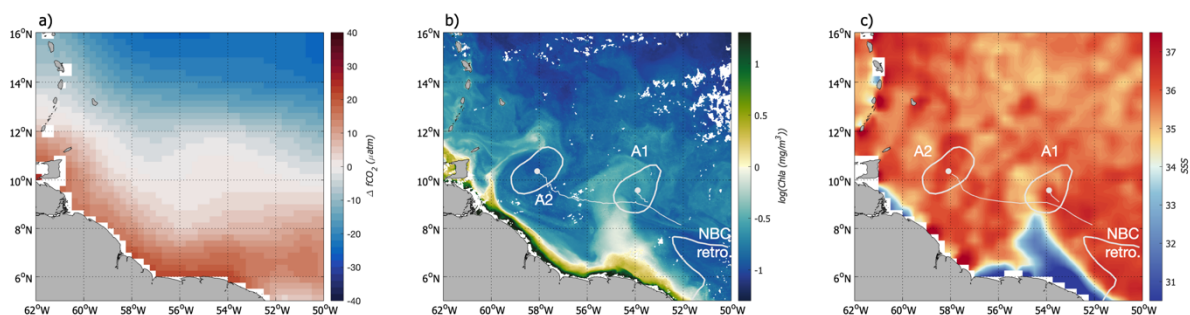


Figure 1: ΔfCO₂ February 1998-2015 climatology (Landschützer et al., 2020). **b)** Chlorophyll-a and **c)** SSS on Feb. 6th with the
105 contours of NBC rings A1 and A2 defined by the TOEddies algorithm (Laxenaire et al. 2018) from concurrent satellite Absolute
Dynamic Topography (ADT) field, their center and trajectory. The 0.51 m contour of satellite derived ADT represents the NBC
retroflexion.

The paper is organized as follows. We present the in-situ observational data from the EUREC⁴A-OA/ATOMIC experiment as
110 well as the satellite data in section 2. We identify the water masses observed in the region, their physical and biogeochemical
properties and estimate the CO₂ fluxes at regional scale using empirical relationships in section 3. We compare the results with
climatologies of CO₂ fluxes to evaluate the added knowledge brought by the intensive surveys of February 2020 and discuss
the interannual variability in section 4 followed by the conclusion.

2 Data and Methods

115 2.1 In-situ data

The EUREC⁴A-OA (Elucidating the Role of Clouds-Circulation Coupling in Climate Ocean-Atmosphere) / ATOMIC
(Atlantic Tradewind Ocean Mesoscale Interaction Campaign, Stevens et al., 2021) campaign took place in January and
February 2020 and involved research vessels (RV) from France (RV Atalante, Speich & The Embarked Science Team, 2021),
Germany (RV Maria S. Merian, hereby designated as Merian, Karstensen et al., 2020 and RV Meteor, not considered in this
120 study since no CO₂ measurements were taken onboard), and the United States (RV Ronald H. Brown, hereby designated as
Ron Brown, Quinn et al. 2021). These cruises provided numerous in-situ measurements and, in this study, we will focus on
the continuous near surface measurement of temperature, salinity, fCO₂ and winds.



Temperature, salinity from thermosalinographs (TSG), as well as $f\text{CO}_2$, were measured from water pumped ~ 5 m below the surface (Figure 2 a,b,c, $\Delta f\text{CO}_2$ from measured $f\text{CO}_2$). For each ship, the resulting CO_2 data is corrected (Lefèvre et al., 2010; Pierrot et al., 2009) from the temperature difference between the water at the ship's water intake and the one analyzed by the instrument. On RV Atalante, underway oceanic and atmospheric $f\text{CO}_2$ were detected by infrared detection using a Licor 7000 (Olivier et al., 2020). The $f\text{CO}_2$ system was the same as in Lefèvre et al. (2010). It uses an air-sea equilibrator described by Poisson et al. (1993). Seawater from the TSG pumping circuit circulates in the equilibrator at a rate of $2 \text{ L}\cdot\text{min}^{-1}$. A closed-loop of about 100 ml of air flows through the equilibrator designed to avoid bubbles at the air-sea interface. To minimize temperature corrections, the equilibrator is thermostated with the same seawater as the one used for CO_2 measurements. The temperature difference between the equilibrator and the sea was on the order of $0.5 \text{ }^\circ\text{C}$.

Furthermore, 138 samples for dissolved inorganic carbon (DIC) and total alkalinity (TA) analysis were collected onboard RV Atalante as well as inorganic nutrients (silicate, phosphate, nitrate and nitrite).

An OceanPackCUBE ferrybox system from SubCtech was installed on the RV Merian measuring continuously the oceanic $f\text{CO}_2$. Water is pumped at a rate of $\sim 7 \text{ l}/\text{min}$ through a debubbler unit subsequently followed by a SeaBird SBE 45 thermosalinograph before it circulates along a membrane through which CO_2 diffuses. On the other side of the membrane, the air-loop is circulated at a rate of $0.5 \text{ l}/\text{min}$ through a Li-COR LI840 non-dispersive infrared gas analyzer (e.g., Arruda et al., 2020). On RV Ron Brown the General Oceanic Inc. 8500 $p\text{CO}_2$ instrument follows a similar methodology to the underway $f\text{CO}_2$ system deployed on the Atalante and is detailed in Pierrot et al. (2009).

Wind measured by the weather stations of each research vessel is adjusted using a logarithmic wind velocity profile to represent the wind at 10 m height above sea level which is used to compute the air-sea CO_2 fluxes.

An intercomparison of the $f\text{CO}_2$ measured by the RVs Atalante and Merian is attempted when the ships were located at a distance inferior to 5 km (Figure 2d). On average, the $f\text{CO}_2$ measured by the RV Merian is $6.4 \mu\text{atm}$ higher than the one measured on the RV Atalante, with a standard deviation of $4.8 \mu\text{atm}$. The RVs Merian and Ron Brown crossed the same water mass at $13\text{--}14^\circ\text{N}/57^\circ\text{W}$ on February 12th. On average, the RV Merian $f\text{CO}_2$ is $6 \mu\text{atm}$ higher than the RV Ron Brown $f\text{CO}_2$. In part we link these differences to the slower response time of the membrane system, however differences also lie within the uncertainties of the $f\text{CO}_2$ observing systems ($\sim 5 \mu\text{atm}$ for the membrane system installed on the RV Merian (see Arruda et al., 2020) and $\sim 2 \mu\text{atm}$ for the equilibrator systems installed on the RVs Atalante and Ron Brown). The region where RV Merian and RV Atalante were very close is very variable (standard deviation of $20 \mu\text{atm}$), and the RV Merian and RV Ron Brown were never in the same place at the same time, so that the observed differences could also be due to the natural variability of $f\text{CO}_2$ sampled differently by the various ships. Hence, we did not apply any correction and we checked that the effect of a $6 \mu\text{atm}$ systematic bias on the RV Merian $f\text{CO}_2$ has a minor effect on our resulting interpolations. It would lead to less than $2 \mu\text{atm}$ difference on our mean interpolated $f\text{CO}_2$ and less than $0.1 \text{ mmol}\cdot\text{m}^{-2}\cdot\text{day}^{-1}$ on the mean derived air-sea CO_2 flux.

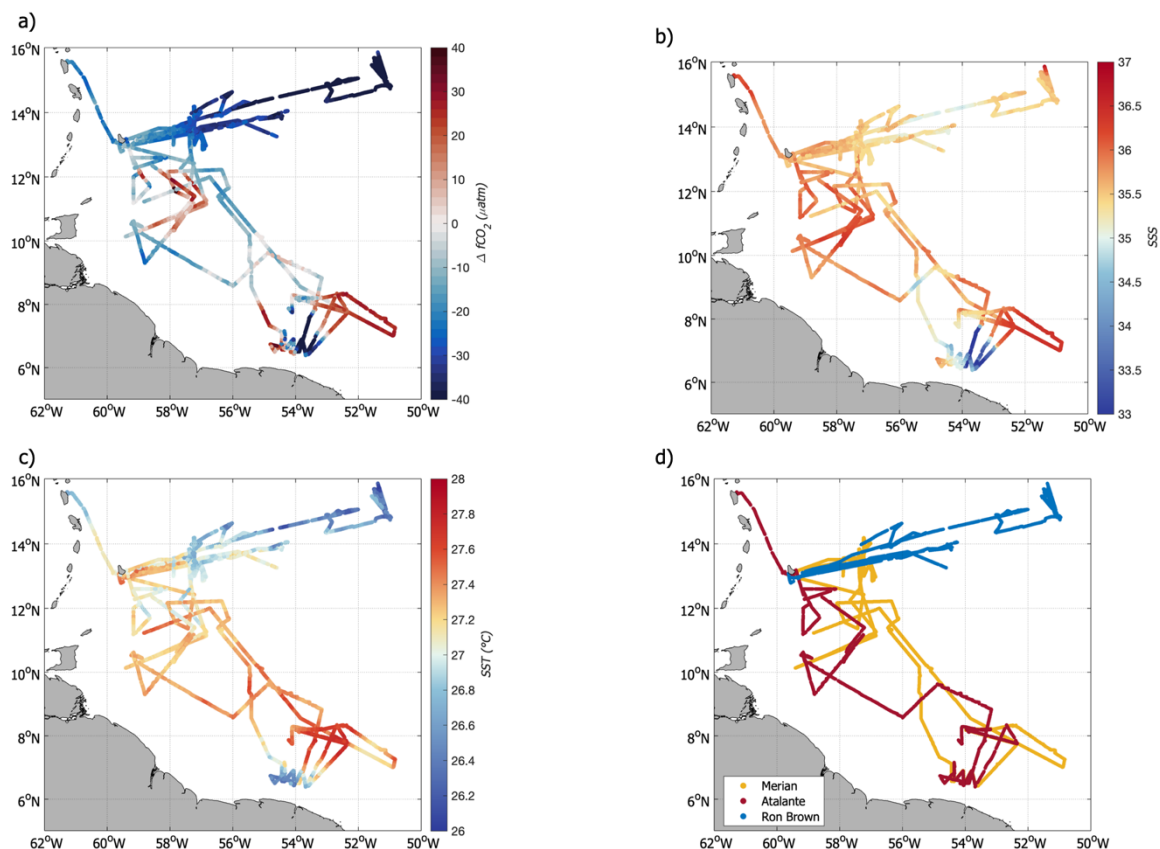


Figure 2: In-situ measurements of surface (a) $\Delta f\text{CO}_2$, (b) salinity and (c) temperature. The Merian, Atalante and Ron Brown ship tracks are presented in (d).

2.2 Satellite and atmospheric reanalyzes data

160 Daily satellite maps of chlorophyll-a (Chl_a), sea surface temperature (SST), as well as absolute dynamic topography (ADT) and sea surface salinity (SSS) are used in this study.

The salinity maps are a blend of the Soil Moisture Ocean Salinity (SMOS, Jan. 2010-present), and Soil Moisture Active Passive (SMAP, Apr. 2015-present) measurements developed by Reverdin et al. (2021) and optimized for the northwestern tropical
165 Atlantic in February 2020 (Figure 1c). The European SMOS and US SMAP missions observe the sea surface by L-band radiometry from sun-synchronous polar-orbiting satellites (Entekhabi et al., 2010; Font et al., 2009; Kerr et al., 2010; Piepmeier et al., 2017). Combining 6 a.m. and 6 p.m. measurements of both missions provides an almost complete coverage each day.



When the coverage was not complete over our region, the 6 a.m. track of the following day was also included. This daily field is available for the first 20 days of February, and leaves out only 2 days without sufficient coverage to retrieve salinity data. It has a spatial resolution close to 70 km, and an uncertainty on the order of 0.5 pss. The product, its uncertainties and the comparison between the TSG salinity and the SSS product are detailed in Reverdin et al. (2021).

Daily Chl_a concentration maps and SST maps are produced by CLS (Stum et al., 2016) on a spatial grid of 0.02°. The Chl_a concentration maps are composites built from VIIRS (on Suomi-NPP and NOAA-20 US platforms) and OLCI (on Sentinel 3A and 3B Copernicus European platforms) satellite sensors. The SST product is a 1-day average of 4 infrared radiometer satellite data. Both datasets are sensitive to the cloud cover, but during our period of interest, they are usually without many gaps except at the end of February. Comparison between the TSG SST and the satellite SST product are detailed in the RV Atalante cruise report (Speich & The Embarked Science Team, 2021).

Daily ADT maps at a ¼° resolution combine data from all satellites available for the period 1993 to present. From these ADT maps, the TOEddies algorithm, developed by Laxenaire et al. (2018), identifies eddies and their trajectories (Figure 1). The eddy detection is based on the closed contours of ADT, as well as the maximum geostrophic velocity associated to the eddy.

In order to compute the air-sea CO₂ fluxes, the European Centre for Medium-Range Weather Forecasts (ECMWF) Reanalysis v5 (ERA5) hourly wind speed and mean sea level pressure, P_{atm}, is used. ERA5 covers the period from January 1950 to present, and provides hourly data on a 30 km grid. In addition, the monthly wind speed and SST fields over the period 1998-2015 are used, and a climatology over this period is computed. The wind speed in the region in winter is on average between 6 and 8 m/s and its variability is low.

We compare the EUREC⁴A-OA/ATOMIC observations with the observation-based CO₂ partial pressure (pCO₂) climatology developed by Landschützer et al., (2020), created using a 2-step neural network method (Landschützer et al., 2016) and combining open and coastal ocean datasets. The associated ΔpCO₂ and air-sea CO₂ flux monthly field climatologies over the 1998-2015 period are computed using the ERA5 climatological wind, SST and P_{atm} fields as well as the atmospheric CO₂ from the Ragged Point, Barbados station.

2.3 Methods

2.3.1 Air-sea CO₂ flux

We compute the air-sea flux (F ; mmol.m⁻².day⁻¹) as:

$$F = k \cdot K_0 \cdot (fCO_2 - fCO_{2atm}) \quad (2)$$



Where K_0 is the solubility of CO_2 in seawater, expressed as a function of SSS and SST by Weiss (1974); $f\text{CO}_{2\text{atm}}$ is the atmospheric CO_2 fugacity; and k is the gas transfer velocity. k is calculated following the relation from Wanninkhof (2014):

$$k = 0.251 \cdot \langle U^2 \rangle \cdot (Sc/660)^{-0.5} \quad (3)$$

where Sc is the Schmidt number and U is the wind speed at 10 m above sea level measured by each ship's weather station or derived from ERA5 wind speed. The measured winds from the ships are used to compute the along-track flux, while the ERA5 wind speed is used for the satellite-based analysis and the air-sea CO_2 flux climatology.

In order to compute $f\text{CO}_{2\text{atm}}$ over that period, we first derived the saturation vapor pressure ($P_{\text{H}_2\text{O}}$) then the atmospheric $p\text{CO}_2$ using the monthly averaged CO_2 mole fraction ($x\text{CO}_{2\text{atm}}$) measured at the NOAA/Earth System Research Laboratory (ESRL) station in Ragged Point, Barbados (13.17°N, 59.43°W):

$$f\text{CO}_{2\text{atm}} = x\text{CO}_{2\text{atm}} \cdot (P_{\text{atm}} - P_{\text{H}_2\text{O}}) \cdot C_f \quad (1)$$

Where $P_{\text{H}_2\text{O}}$ is the saturation vapor pressure computed from SSS and SST, and C_f is the fugacity coefficient, function of the atmospheric pressure and SST (Weiss, 1974).

2.3.2 Reconstruction of $f\text{CO}_2$ from satellite maps

We observed that in the northwestern tropical Atlantic in winter the in situ $f\text{CO}_2$ strongly depends on SST, SSS and surface $\text{Chl}a$ (Figure 3). There is a strong positive dependence of $f\text{CO}_2$ on SSS, with low $f\text{CO}_2$ for low SSS (Figure 3a). Across the whole EUREC⁴A-OA/ATOMIC region, SST did not vary much (mean SST of 27°C, and standard deviation of 0.5°C), but warmer waters present higher $f\text{CO}_2$. The dependence on $\text{Chl}a$ allows for the discrimination of water masses with the same surface TS properties but not the same $f\text{CO}_2$. $f\text{CO}_2$ is not only influenced by ocean dynamics and chemistry, but also by marine biology. The biological carbon pump is one of the major components of the oceanic and global carbon cycles, as the photosynthetic production of organic carbon by marine phytoplankton accounts for about half of the carbon fixation associated with global primary production (Arrigo, 2007; Behrenfeld et al., 2006; Field et al., 1998). Satellite-based $\text{Chl}a$ is hard to discriminate from detrital material in areas where both are present and have the same wavelength. Figure 3 shows that waters with a SST of 26.5°C and SSS between 35-36 can either be rich in $\text{Chl}a$ and have a high $f\text{CO}_2$ or low in $\text{Chl}a$ and have a low $f\text{CO}_2$. Waters rich in detrital material tends to limit the phytoplankton growth and microbial respiration of riverine material on the continental shelf likely dominates (Aller & Blair, 2006; Medeiros et al., 2015; Mu et al., 2021). This relationship is analyzed in more detail for the different water masses identified in the region in parts 3.2. and 3.3. $\text{Chl}a$ was not measured onboard, thus, we use satellite surface $\text{Chl}a$ co-located along the ship track.

Our approach is to derive from this large dataset a relationship linking $f\text{CO}_2$ to SST, SSS and $\text{Chl}a$ in order to provide maps of $f\text{CO}_2$ based on the satellite maps of SST, SSS and $\text{Chl}a$. Even considering the extent of the EUREC⁴A-OA atomic cruise, the dataset is still sparse, and cannot fully represent the small-scale variability it highlights. In order to understand the fluxes at regional scale the need for a good spatial resolution arises. For that, the surface T-S- $\text{Chl}a$ diagram computed from the ship



measurement (and collocated satellite *Chla*) is interpolated using a linear 3D interpolation on a grid of SST, SSS and *Chla*. The grid has a resolution of 0.01°C in SST, 0.1 in SSS, and 0.01 in log(*Chla* (mg/m³)). Using a 3D linear interpolation to mapping the fCO₂ data over a grid is a simple yet effective solution for a dataset that is still relatively sparse. The method is presented in more details in the supplementary materials (Text S1). Using a linear fit prevents from oscillations between two data points, and yields good results. Along the ship track, the standard deviation between the measured and reconstructed fCO₂ is of 4 μatm. To each triplet of surface T, S, and log(*Chla*) in the range of the values measured by the ship is therefore associated a value of fCO₂ based on the 3D linear interpolation of the in-situ values. In order to cover the whole range of T-S-log(*Chla*) present in the region, we extrapolate to lower temperatures and lower salinities than the ones measured by the ship. In order to do so, we add 4 points to the T-S-*Chla* diagram at lower salinities and lower temperatures based on previous knowledge of the region. For the low salinity domain (SSS < 30), fCO₂ is strongly dominated by salinity and the influence of temperature is weak (Lefèvre et al., 2010). The SSS-fCO₂ relation developed by Lefèvre (2010) is in good agreement with the SSS-fCO₂ relationship computed from this study data (supplementary Figure S1) in the common range, we therefore use it to compute fCO₂ at a salinity of 26 (fCO₂(S = 26) = 251.4 μatm). The lower temperature is mostly located in the northern part of the domain, that is the least variable and where the variations of fCO₂ are dominated by the ones in temperature. From this dataset

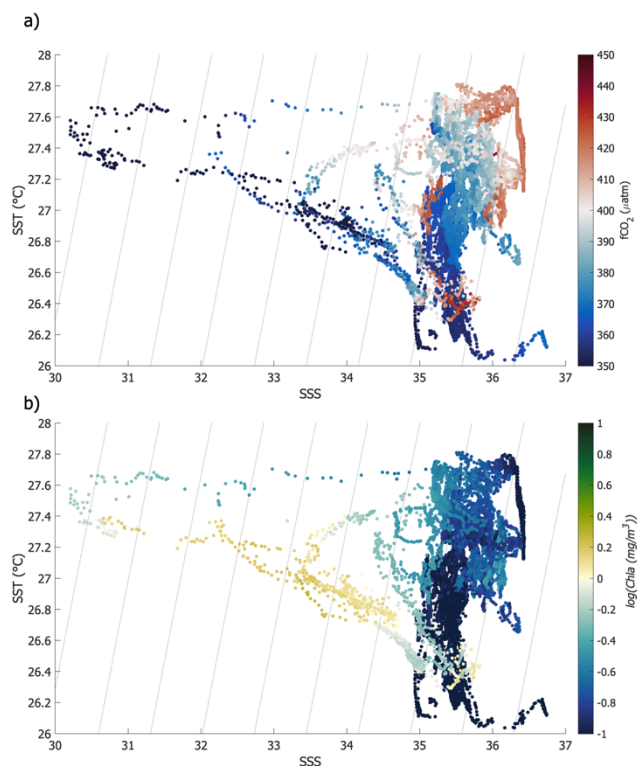


Figure 3: Surface TS diagram, color-coded with fCO₂ (a) and *Chla* (b).



we compute a variation of $15 \mu\text{atm}/^\circ\text{C}$, which is consistent with the $4.23\% \text{ }^\circ\text{C}^{-1}$ expected variation of $f\text{CO}_2$ with temperature due to the temperature sensitivity of the carbonate dissociation constants and CO_2 solubility (Takahashi et al., 2002; Wanninkhof et al., 1999). We use this dependency to compute the $f\text{CO}_2$ at a temperature of 24°C to extend cover the whole range of temperature in the region.

250

We combine the interpolated $f\text{CO}_2$ with satellite maps of SST, SSS and $\text{Chl}a$ to obtain daily high-resolution maps of $f\text{CO}_2$. Some days, either the presence of clouds altering the $\text{Chl}a$ and SST or the lack of salinity coverage prevent the retrieval of $f\text{CO}_2$. In order to limit the error on $f\text{CO}_2$, we only keep 9 days out of the 20 first days of February (2, 4, 6, 7, 9, 11, 12, 17 and 19 of February) where the coverage is sufficient. Then, daily mean sea level pressure maps and wind fields are used to compute the air-sea CO_2 flux over the region in a similar way as described in 2.3.1. The salinity maps present major errors near islands, because no correction of the island effect on the SMAP maps (Grotsky et al., 2018) was applied. Therefore, the reconstructed flux will be studied over a region excluding the close vicinity of the islands [59°W - 50°W , 5°N - 16°N].

260 3 Results

3.1 A transition region presenting a strong mesoscale activity

Figure 2a presents the $\Delta f\text{CO}_2$ measured during the EUREC⁴A/ATOMIC campaign in January-February 2020. It shows a complex environment that presents similar large-scale features as the climatology, but it reveals numerous smaller scale structures (Figure 1a). Among the latter, two stand out. These are the very low $f\text{CO}_2$ in the south-eastern part of the domain, and the high $f\text{CO}_2$ around 11°N . Winter is often considered as a period of low variability in the western tropical Atlantic, however, it is still a highly dynamic region. The northwestern tropical Atlantic is commonly divided into two parts, the northern much less variable part (also called “Trade wind region”), and the southern part, also referred as Eddy Boulevard (Stevens et al., 2021). In early 2020, the NBC retroflection was very variable and shed two large anticyclonic rings (Figure 1b,c). They are long-lived 250-km large eddies traveling north-westward toward the Caribbean in the Eddy Boulevard region. The ring detection algorithm TOEddies based on ADT indicates that NBC ring A2 separated from the retroflection in late December, was fairly stationary during the cruise period (February 2020) and located around 58°W - 11°N . NBC ring A1 separated from the retroflection in early February 2020 and then stayed around 54°W - 10°N for 10 days before translating northwestward toward the Caribbean after the 20th of February. These eddies contribute to the variability of the region in two ways. As they travel, they transport the water trapped in their core during their formation, but they also stir the surrounding waters.

270



275 3.2 Surface water masses identification

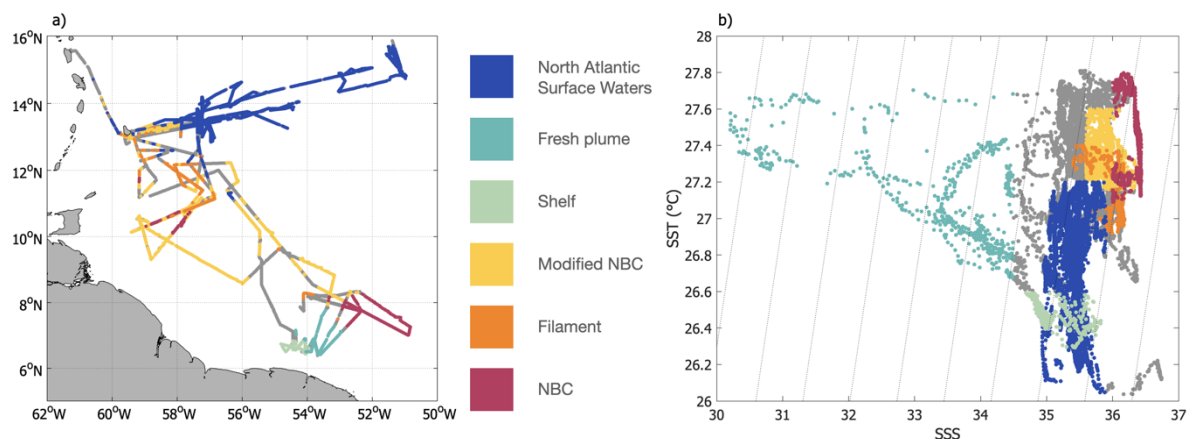


Figure 4: a) Map representing the RVs *Atalante*, *Merian* and *Ron Brown* ship tracks color-coded with the identified water masses. b) T-S diagram color-coded with the water masses; the gray color corresponds to points that do not fit into the definition of the identified water masses.

280

In order to better understand the variability of the region, it is necessary to characterize the main water masses present in winter. From SST and SSS only, we are not able to define water masses with a unique $f\text{CO}_2$ signature (Figure 3). By combining SST and SSS with $\text{Chl}a$ and using information from the dynamical structures of the region, we identified six upper-ocean water masses (Figure 4). For example, the fresh plume water mass corresponds to low SSS, while the NBC water mass is associated to warm SST, high SSS and low $\text{Chl}a$ (Figures 3 and 4) in the region of the retroflexion and eddy formation. The along track $\Delta f\text{CO}_2$ for each ship is presented on Figure 5, color-coded with the identified water mass, highlighting the link between the surface T-S- $\text{Chl}a$ relation and $\Delta f\text{CO}_2$. In this first part, we will present the two surface water masses that are usually identified in the region (e.g. Longhurst et al., 1995, 2010) and their physical properties. We will introduce four new ones in the following parts, as well as their associated dynamic structures.

290 North of Barbados, the domain is mostly dominated by North Atlantic Subtropical Waters. They have a SSS in the range of 35 to 36 and are relatively cold ($\text{SST} < 27.2^\circ\text{C}$). Their SST diminishes over time towards the end of February. These waters are less influenced by coastal dynamics and therefore are not very productive at the surface ($\text{Chl}a$ levels inferior to $0.14 \text{ mg}\cdot\text{m}^{-3}$) due to low nutrient levels. They are mainly located north of 13°N , and get progressively colder toward the north-east. The RV *Ron Brown* stayed in that Trade Wind region for almost a month (Figure 5). The observations collected from this ship show NASW lower $f\text{CO}_2$ with respect to the atmosphere ($\Delta f\text{CO}_2 = -40 \mu\text{atm}$). Similar results are found on one of the RV *Merian*'s transect, with $\Delta f\text{CO}_2 < -30 \mu\text{atm}$.

The surface-intensified NBC is fed by the central branch of the South Equatorial Current (SEC, Schott et al., 1998). As the cold and saline water from the upwelling region is transported westward by the SEC, it warms up ($\text{SST} > 27^\circ\text{C}$), but retains its saline characteristic ($\text{SSS} > 36$) as it reaches the NBC retroflexion region (Figure 4). This NBC water mass is oligotrophic



300 (Figure 3b), and therefore in our area of interest distinguished itself by its low level of surface $Chla$ ($Chla < 0.14 \text{ mg}\cdot\text{m}^{-3}$). These waters are found in the retroflexion area, and sampled by both RVs Merian and Atalante at the beginning of February (Figure 5).

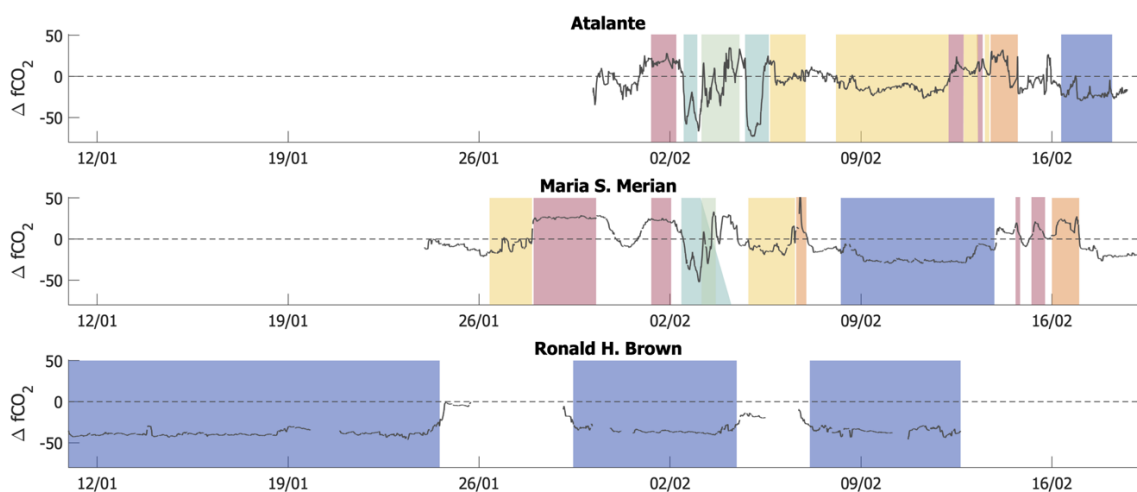


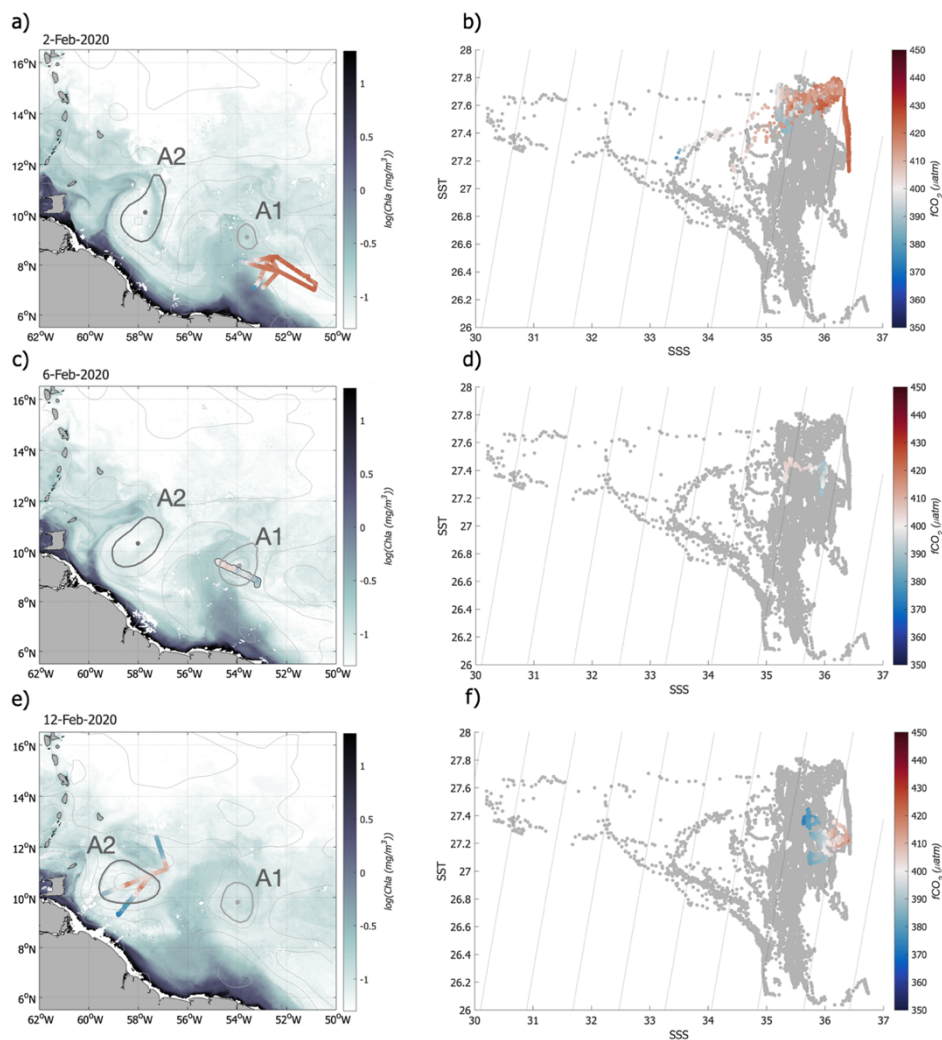
Figure 5: RVs Atalante (top), Merian (middle) and Ron Brown (bottom) ΔfCO_2 time-series. The background color indicates the crossed water mass domains (see definition in legend of Fig 4).

3.3 North Brazil Current rings

305 The extension of the NBC retroflexion varies depending on the state of eddy formation. It moves northwestward up until 9°N as an eddy is forming, and then retracts to the southeastern part of the region. During our period of interest, the retroflexion shed anticyclone A1 at the beginning of February. It is difficult to estimate the date of shedding as the area is highly dynamic and detecting the first closed contour of ADT is complicated and may be inaccurate. It is however interesting that the two ships sampled the retroflexion when it was expanding to generate A1, and this northwestward expansion is well observed on several
310 physical and biogeochemical parameters (Figure 6a). RV Merian crossed the retroflexion on January, 27th and stayed in the area until February, 2nd (Figure 5). $Chla$ present on the shelf is advected by the strong currents on the periphery of the retroflexion and delineates well its south-western side (Figure 6a). The NBC waters stand out on the surface TS diagram, as they are the most saline waters observed in the region (Figure 6b). They are also high in fCO_2 which reflects their equatorial origin. Their SST is relatively warm, varying from 27.8°C at the crossing of the first retroflexion front, to 27.2°C . The region
315 is rather homogeneous, with an almost constant SSS of 36.3 and ΔfCO_2 along the multiple crossings, as observed on the Merian and Atalante transects (Figure 5). On average along those transects, the NBC fCO_2 is higher than fCO_{2atm} by $20 \mu\text{atm}$.



Anticyclone A1 is further crossed by the RV Atalante on February 6th, just a few days after its separation from the retroflection (Figure 6c). The surface signal is almost lost, both in SST and in $f\text{CO}_2$ (Figure 6cd). It is mainly composed of modified NBC water, which properties are close to the NBC water (high SSS, high SST, low Chla) but not as pronounced. This water mass covers a larger area, which mainly encompasses the Eddy Boulevard region. It is defined here as $\text{SSS} > 35.6$, $27.16^\circ\text{C} < \text{SST} < 27.6^\circ\text{C}$ and $0.11 \text{ mg m}^{-3} < \text{Chla} < 0.25 \text{ mg m}^{-3}$. While the high Chla water delimits the retroflection area, it partly covers the eddy A1.



325 **Figure 6:** a) RVs Atalante and Merian ship track in the NBC retroflection (Merian: Jan. 27th to Feb. 2nd, Atalante: Feb 2nd), c) in NBC ring A1 (Atalante: Feb 6th) and e) in NBC ring A2 (Atalante: Feb 12th-13th, Merian: Feb 13th-14th) color-coded with $f\text{CO}_2$. The background represents the Chla on Feb 2nd (a), Feb 6th (c) and Feb 12th (e), and the contours of NBC rings A1 and A2 are indicated. b),d),f) Corresponding T-S diagrams color-coded with $f\text{CO}_2$.



330

NBC ring A2 presents a different situation. Detached from the retroflection in early December 2019 (as defined from altimetry detection), it travelled north-westward while retaining an intense coherent core. Coastal waters identified by their high Chla content were less present and mostly entrained at the north-westward edge of the eddy. After two months, A2 almost reached Trinidad and Tobago and was located around 11°N/58°W when it was sampled by the two ships (Figure 6e). The SST signal is eroded, and most of the eddy is mostly made of modified NBC water with relatively low fCO₂. However high SSS (36.5) and fCO₂ (415 μatm) are still visible near the eddy center on the two crossings made by RV Atalante on the 12th and 13th of February. This is confirmed by the two sections of the Merian that crossed the altimetric eddy center and measured SSS 0.5 higher in the 50 km radius around the center and above 36. The NBC water mass is therefore found close to the center of eddy A2, as well as its associated high fCO₂.

340

From the collected observations, it appears that the surface signature of NBC rings is relatively variable and complex. It is well marked in their formation area in the NBC retroflection, where waters brought north by the NBC are warmer, saltier, and higher in fCO₂ than the water of the northwestern tropical Atlantic. As the eddies travel northwestward, further away from the retroflection, they may be subject to various processes that modify the surface signal. Unfortunately, the data collected is not sufficient to shed light on which processes involved in this situation. South of Barbados, away from the retroflection, the modified NBC is therefore the most common water mass. Nevertheless, the NBC water is still sometimes observed months after the separation from the retroflection, in the eddy center.

345

3.4 Freshwater plume

The NBC rings form and evolve in an area highly influenced by the Amazon River plume. Even if February is a period of low Amazon River outflow (Dai & Trenberth, 2002), freshwater events are relatively common. In February 2020, a freshwater plume detached from the Guiana plateau and spread out into the northwestern tropical Atlantic. The off-shelf plume was steered northward by the retroflection and NBC ring A1 up to 12°N and then extended westward toward the Caribbean Sea. Waters carried by the plume strongly contrast with the saline waters of the retroflection. They include water from the Amazon and present low SSS (SSS < 34.5), low fCO₂ (fCO₂ < 380 μatm) and high Chla (Chla > 0.25 mg m⁻³). The plume was crossed three times, twice on February 2nd and once on February 5th (Figure 5). Freshwater from the Amazon arrived on the plateau on the 1-2nd of February and was then entrained northwestward by Ekman transport and geostrophic currents (Reverdin et al., 2021). On the 2nd of February RVs Atalante and Merian left the retroflection area to cross the adjacent nascent plume. SSS rapidly decreased, reaching 33 which is associated to a strong decrease of fCO₂ (Figure 7). From the 2nd to the 5th of February, the plume formed and on February 5th the plume is approximately 100 km wide, with lowest salinities around 30. Based on satellite SSS data of the following days, the plume appears to have reached even lower salinities and then spread out over the northwestern tropical Atlantic. It first spread northward, steered by A1 and then northwestward, channeled between A1 and A2

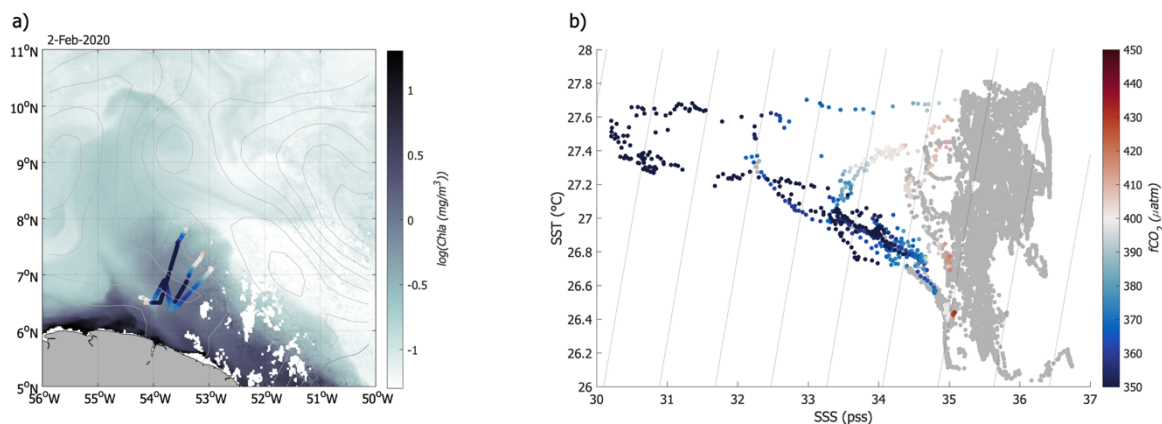
355

360



reaching all the way up to 12°N and extending over more than 100 000 km² (Reverdin et al., 2021). The plume can be followed by satellite SSS and Chla maps (Figures 6a, c, e). Indeed, the low SSS is also accompanied by Chla as water from the Amazon are considered highly productive. The north-western tropical Atlantic is in general nutrient-limited but the nutrients brought by the Amazon can support the occurrence of a bloom. The plume is also characterized by high silicate (between 4 and 10 μmol kg⁻¹ in the plume), while nitrate and phosphate are rapidly consumed. Traces of inorganic phosphorus were observed in the plume, while nitrates were absent from surface waters (Supplementary Figure S2). Low salinity combined with high biological productivity led to low fCO₂ and a strong carbon drawdown in the plume, as the ΔfCO₂ reached -73 μatm on February 5th (Figure 5).

In an area highly influenced by the NBC waters, through rings or the retroflection, the plume stands out and modify the biogeochemical dynamics of the region.



375 **Figure 7: a) RVs Atalante and Merian ship track in the freshwater plume (Atalante: Feb 2nd, Feb 5th, Merian: Feb 2nd) color-coded with fCO₂. The background represents the Chla on Feb 2nd. b) Corresponding T-S diagram color-coded with fCO₂.**

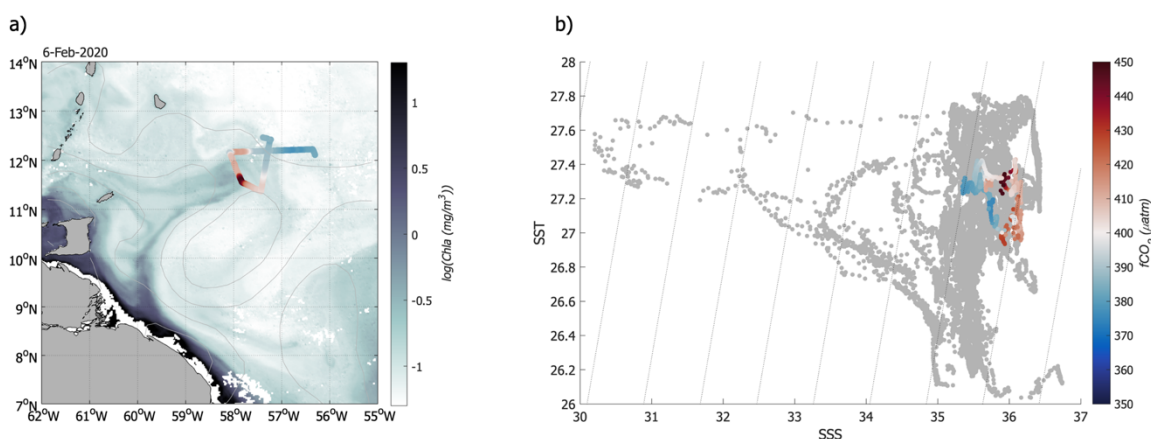
3.5 Coastal water and filaments

The freshwater plume is not the only water stirred by the NBC rings travelling from the NBC retroflection towards the Caribbean. The shelf water is very different from the plume water, and was only sampled sparsely on the way in and out of the plume (Figures 4,5). On the Guiana plateau water is very rich in Chla and detrital material, rather saline (SSS ~ 35.5) and relatively cold (SST ~ 26.5°C) (Figure 4). Since the water sampled on the edge of the plume was cold due to a local upwelling event (or vertical mixing event) detailed in the supplementary materials (Figure S3), temperature is not homogenous on the shelf.

Further north, a filament is stirred on the western side of NBC ring A2 (Figure 8a). It is a small-scale structure, approximately 10 km wide, easily identifiable due to its high Chla. The filament is continuously stirred by A2, and so is already visible on



Chla maps of February 2nd (Figure 6). It followed A2 westward's translation and was crossed on February 6th and 17th by RV Merian, and on February 14th by RV Atalante (Figure 5). It has a SSS close to 36, and an SST between 27°C and 27.5°C, thus it is slightly colder and more saline than its surrounding waters (Figure 7b). It stands out by its high Chla content (Chla > 0.25 mg m⁻³), even if this is lower than close to the coast or in the freshwater plume. The strongest signal is observed on the ocean carbon parameters. In contrast to the freshwater plume, this filament presents very high fCO₂ (> 430 μatm), highlighting different origins. It stands out from the ship track time series by also having a larger positive ΔfCO₂ (50 μatm). Whereas the freshwater plume observed more southeastward carries water recently arrived on the plateau from the Amazon, the northwestward filament contains shelf waters.



395 **Figure 8:** a) RV Merian ship track in the shelf water filament (Feb 6th) color-coded with fCO₂. The background represents the Chla on Feb 6th. b) Corresponding T-S diagram color-coded with fCO₂.

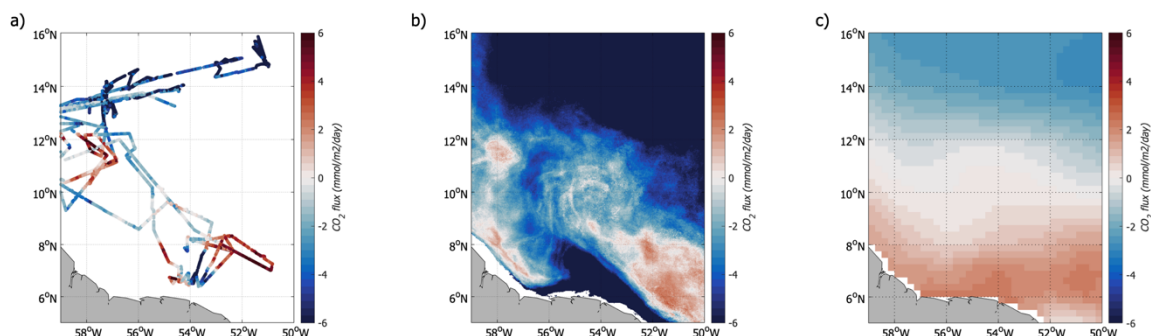
3.6 CO₂ air-sea flux

In order to better characterize the impact of each structure on the regional flux, we computed air-sea CO₂ maps from satellite
400 data, at a resolution higher than 60 km (Figure 9), averaged over the period of the cruise (February 2nd to February 19th). The
along-track flux represented on Figure 9a and the reconstructed regional field (Figure 9b) show the importance of the small-
scale dynamical structures, and highlights two strong regimes that are found on the reconstructed map. The air-sea CO₂ flux
in the northeastern part of the domain, characterized by the NASW, is mainly dominated by temperature effects while further
south the presence of NBC rings, and their interactions with shelf waters, create a strong dependence of the CO₂ flux on SSS
405 and on the biological and biogeochemical processes highlighted by Chla.

We evaluate the integrated air-sea CO₂ flux over the region. In February, waters are the coldest, and the region is a strong CO₂
sink of -1.7 TgC month⁻¹ (Figure 10). Three biogeochemical domains mainly contribute to the air-sea CO₂ flux, the NASW,



the freshwater plume and the NBC retroflection. The impact on the flux of the small-scale coastal filament is evident along the
410 ship tracks (Figure 9b). However, its contribution to the total flux is weak as the signal is smoothed when averaging over
February, as the filament moves following the A2 ring northwestward translation. Each of the main three regions is defined
based on its averaged SST, SSS and Chla properties in February and the region-specific flux is determined (Figure 10).



415 **Figure 9:** a) Air-sea CO₂ flux measured in Jan-Feb 2020 during the EUREC⁴A-OA/ATOMIC cruise. b) Air-sea CO₂ flux
reconstructed over February 2020. c) February climatology of the air-sea CO₂ flux over 1998-2015 (Landschützer et al., 2020).

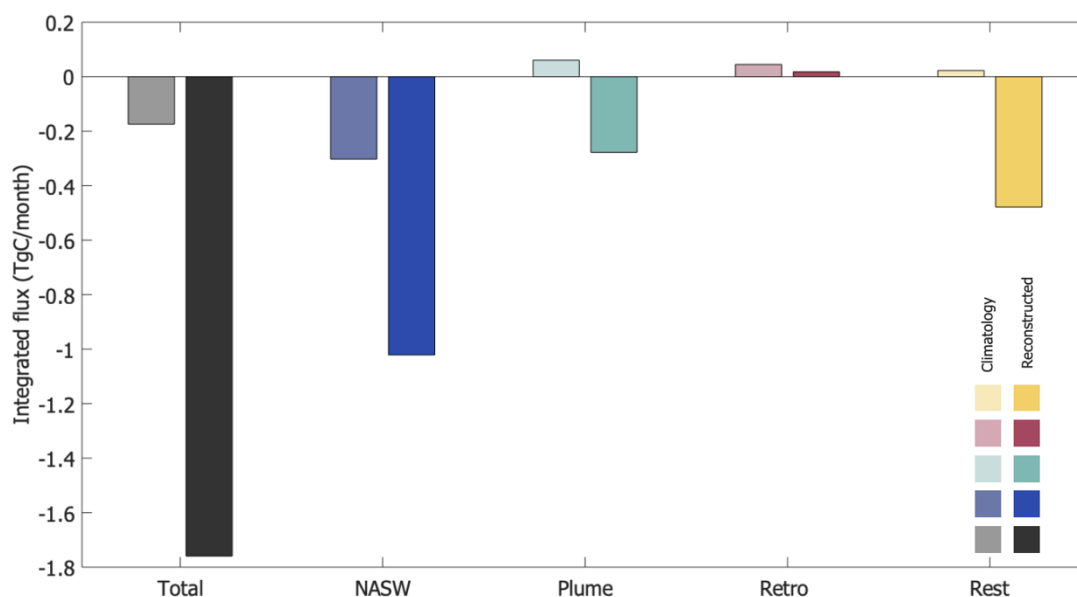
NASW contributes to about 60% of the total sink due to their relatively cold temperature and to strong winds that enhances
the air-sea exchanges. These waters extend from Barbados northward and eastward, cover more than 1/3 of the domain and
420 show a weak variability over the month of February.

The NBC retroflection is a source of CO₂ to the atmosphere. In February, the strongest signal is observed in the southeastern
part of the domain up to 8°N/53°W. The retroflection nevertheless impacts the region as far as 10°N/54°W as it is spatially
variable, reaching up to 10°N when shedding an eddy. NBC rings present a small positive February air-sea CO₂ flux average.
425 Eddy A1 is almost stationary from its formation date (around February 6th) until February 20th and its neutral to slightly positive
CO₂ flux is centered around 10°N/54.5°W (Figure 9). Eddy A2 translates rapidly westward at the beginning of February, and
then northward from the 15th of February. Its signal is therefore not as visible as on the ship tracks as it is averaged over one
month. The retroflection is the main region with a positive air-sea CO₂ flux, even if the region is too small to have a big global
impact, understanding small-scale features may be significant for the total flux. The NBC rings carry part of the signal, which
430 is heavily modified as they travel northwestward. As a result, on average for the month of February only the retroflection
maintains a positive flux, while a large part of the domain dominated by modified NBC waters (non-influenced by the plume)
behaves as a small sink.



435 The freshwater plume with Amazon water is nascent when crossed by the ships (Figure 9b), but is already the strongest signal
of the time-series. As the plume develops, it is entrained by NBC ring A1, then A2 and spreads out into the open ocean, as
observed on SSS and Chla maps. The plume generates a strong CO₂ sink that is amplified by strong winds, and reaches up to
12°N (Figure 9). The freshwater plume covers only 10% of the total area, but contributes to almost 20 % of the sink. In winter,
this region is either not characterized in previous studies, or considered as dominated by high fCO₂ waters brought by the NBC
on the climatology. We observe here that the direct effect of NBC rings in transporting CO₂-rich waters is relatively weak in
440 winter, and the main signal is associated to the filaments they stir.

The north-western tropical Atlantic therefore behaves as a sink of CO₂ in February, driven by the cold north Atlantic
subtropical waters and the Amazon freshwater plume stirred by NBC rings.



445 **Figure 10: Integrated flux for the [5°-16°N, 59-50°W] domain, and for 3 water masses. For each bar duet, the one on the left in faded colors represents the integrated flux from Landschützer et al., (2020) February climatology, while the one on the right is computed from the reconstructed flux. Same color code as in Figure 4.**



450 4 Discussion

4.1 Biogeochemical provinces

In an effort to understand how biogeochemistry is forced by physical processes in the ocean and atmosphere, we used surface Chl_a to complement SST and SSS data in defining surface water masses. Partitioning the world ocean into biogeochemical provinces based on physical, geographical and biological criteria has long been proposed to study and better understand biological processes (Fay & McKinley, 2014; Longhurst et al., 1995; Longhurst, 2010). As reviewed by IOCCG (2009), satellite Chl_a has been widely used to determine biogeochemical provinces, a term coined by Platt et al. (1991) and associated biological primary production but relatively few studies have used such methodologies for mapping air-sea CO₂ fluxes. Recently, Landschützer et al. (2013, 2016) have divided the world ocean into biogeochemical provinces for deriving fCO₂ and air-sea CO₂ fluxes. The way we defined water masses, considering time-varying geographical boundaries, is relatively similar to the one used by Longhurst, and some of the surface water masses compare well with Longhurst (2010) biogeochemical provinces. He identified 3 provinces in the Northwestern tropical Atlantic, The North Atlantic Tropical Gyre province (NATR), the Western Tropical Atlantic province (WTRA) and the Guianas Coastal province. The NATR province is defined as the region north of the North Equatorial Current (12°N-14°N) and east of the lesser Antilles. NATR consistently has the lowest surface Chl_a of the North Atlantic. The North Atlantic Subtropical Waters of this paper represent the same physical and biogeochemical processes as NATR and we found differences in reference to the WTRA and GUIA provinces. WTRA includes geographically the NBC and modified NBC waters. However, while the retroflexion of the NBC is mentioned in the physical characteristics of the WTRA, the eddies are also mentioned in the GUIA province. The GUIA province includes all coastal processes, in this case it can be the freshwater plume, as well as high CO₂ coastal waters, and the NBC rings to a certain extent. The latter emphasizes the need to take into account the finer scale in highly dynamic regions.

470 4.2 Integrated CO₂ air-sea flux

The northwestern tropical Atlantic present a strong seasonal variability of CO₂ air-sea fluxes (Landschützer et al., 2016). In February, waters are the coldest, and the region is a strong CO₂ sink of -1.7 TgC month⁻¹ (Figure 10). This region, located at tropical latitudes but combining characteristics of subtropical waters and river outflow, is difficult to represent in large scale climatologies. Indeed, the sink for the month of February is smaller by a factor 10 in Landschützer et al. (2020), and is also severely underestimated in Takahashi et al., (2009), but the low spatial resolution of this last product doesn't allow for a good quantitative comparison. This region has been rarely observed, and the interannual variability described in Landschützer et al., (2020)'s climatology is therefore rather uncertain. The compensating effect of different years cannot explain entirely the difference of signal observed in February 2020 with respect to the two climatologies.

480 Three water masses mainly contribute to the air-sea CO₂ flux, the NASW, the fresh plume and the NBC retroflexion. The NASW contributes to about 60% of the total sink and are not well captured in climatologies, with noticeable differences of



more than 20 μatm between the measured $\Delta f\text{CO}_2$ in 2020 and the one computed from Landschützer et al., (2020) and Takahashi et al., (2009) (the closest grid point is considered for this comparison). The retroflexion is the main region with a positive air-sea CO_2 flux. Its influence is observed up to 10°N - 55°W , but its area is small so its impact on the regional flux is weak. The positive flux of the retroflexion is slightly overestimated in the climatologies, but it could also be due to the difficulty to detect the retroflexion at the beginning of February. The main difference is that the NBC waters rich in CO_2 are localized in the retroflexion area, and are heavily modified when spreading into the Eddy Boulevard.

The freshwater plume is a feature previously not well described for this region in winter and we found a contribution of almost 20 % to the sink. The impact of the Amazon River has been overlooked so far in winter, but it accounts for a large part of the salinity and biogeochemical variability. Freshwater from the Amazon is not just located on the shelf, but it can spread northward advected by the strong currents variability associated to the NBC rings (Reverdin et al., 2021). These rings are the largest, faster rotating and are the most energetic during boreal winter compared to other seasons (Aroucha et al., 2020). Combined with a seasonal increase in the Amazon's outflow, it induces a large variability in SSS, $\text{Chl}a$ and $f\text{CO}_2$. The occurrence of freshwater export from the shelf to the open ocean has a strong influence on the salinity and therefore on the mixed layer depth and air-sea heat exchanges (Reverdin et al., 2021). It also strongly impacts the biogeochemistry of the region as the low $f\text{CO}_2$ is both due to the low salinity of the plume waters and to the biological activity. The plume stirred into the open ocean by the NBC rings brings nutrients in a region strongly nutrient-limited, and generates a local winter bloom. This in turns plays an important role on the air-sea CO_2 flux, and is a crucial feature of the southern part of the northwestern tropical Atlantic.

4.3 Extension to other years and interannual variability

Few tropical Atlantic measurements of biogeochemical tracers are available, in particular in the northwestern tropical Atlantic. The EUREC⁴A-OA/ATOMIC campaign provides the first in-situ comprehensive measurements of $f\text{CO}_2$ in this region for the boreal winter season. The reconstruction of $f\text{CO}_2$ maps likely provides a good understanding of the spatial evolution of $f\text{CO}_2$ and air-sea CO_2 fluxes, and is fitted for the months of January-February 2020. Although the processes described here are specific to winter and thus cannot be extended to other seasons, they will be useful to understand the winter variability of other years.

Only a few cruises cross the region according to the SOCAT database between 2010 and 2019 (period with satellite SSS data) and investigating inter-annual variability is not possible. However, we can test the relation developed for 2020 for other years by using select cruises from the SOCAT database. We thus first use the relationship to reconstruct $f\text{CO}_2$ along the ship tracks (using in-situ SSS and SST and colocalized $\text{Chl}a$) and then over the whole region based on satellite products (OSTIA SST, Globcolour $\text{Chl}a$, SSS+CCI, detailed in the appendix A). A comparison between the measured and reconstructed $f\text{CO}_2$ for the water masses sampled by the SOCAT cruises (NASW, fresh plume, NBC retroflexion, modified NBC) is presented in the appendix (Table A1). Good agreement is found between the $f\text{CO}_2$ from the SOCAT database and the one reconstructed from the in-situ temperature and salinity, and colocalized $\text{Chl}a$ for the four water masses (averaged difference of $5.5 \mu\text{atm}$). When



515 comparing reconstructed $f\text{CO}_2$ maps with $f\text{CO}_2$ on ship tracks (Figure A1), the agreement between $f\text{CO}_2$ in various water
masses is very clear, even though the spatial structures are sometimes a bit misplaced. This is attributable to the slightly coarser
resolution of satellite products not designed specifically for each campaign, to the high spatio-temporal variability of $f\text{CO}_2$ and
to missing *Chla* and SST observations in cloudy areas. February 2020 was mainly cloud free, so that we were able to use high
resolution daily SST and *Chla*. The SSS product used in 2020 is also a daily product. However, for the other years, the satellite
520 CCI *Chla* (if clouds) and SSS products have a weekly temporal resolution, which smear the fast-moving structures. The
gradients between water masses are therefore not always well represented, but we find a good agreement between the $f\text{CO}_2$ of
each structure, which is encouraging for future studies on interannual variability in winter.

By identifying the main processes responsible for the variability of the air-sea CO_2 flux in 2020, we can better understand the
525 interannual variability of the region. Indeed, each of the main water mass has its own interannual variability that shapes the
 CO_2 variability. The northern part of the domain is dominated by the variation of temperature, and therefore its interannual
variability is linked to the one of SST. From 32 years monthly mean SST data, the SST standard deviation in the area is
relatively weak, and doesn't exceed 0.5°C . The northern sink of CO_2 is therefore rather similar from year to year, coherent
with the low standard deviation of the air-sea CO_2 flux computed from Landschützer et al., (2020).

530 As previously stated, most of the variability occurs south of Barbados. The freshwater plume sampled during EUREC⁴A-OA
is a common feature in February. During the 2010-2019 period, events of freshwater reaching the open ocean were observed
each year, and freshwater plumes similar to the one described in this paper were observed during 7 out of 10 years from satellite
salinity data (Reverdin et al., 2021). Two of the main mechanisms driving the occurrence of the plume are the winds near the
Amazon estuary that can induce along shelf transport to the Guyana plateau and the presence of NBC rings. This region is
535 commonly crossed by several NBC rings during winter (Jochumsen et al., 2010; Johns et al., 2003; Mélice & Arnault, 2017)
but it also is subject to a strong year to year variability that has linkages with the variability of the Amazon River outflow
(Aroucha et al., 2020). Therefore, identifying and understanding the processes happening in 2020 should contribute to better
assess the interannual variability of $f\text{CO}_2$ as well as air-sea CO_2 fluxes in the northwestern tropical Atlantic during winter.
Using a combination of SSS, SST and *Chla* brings information on the biogeochemistry of the area in winter and represent well
540 the mesoscale structure.

5. Conclusion

The EUREC⁴A-OA/ATOMIC campaign provides for the first time synoptic measurements related to the air-sea fluxes of CO_2
in the northwestern tropical Atlantic in winter. Six main surface water masses are identified, one of them north of Barbados
(North Atlantic Subtropical Water), and the other five (the NBC retroflexion, modified NBC waters, the freshwater plume,
545 the shelf water and the shelf filament) south of Barbados. The investigation highlights the two different regimes of the region.
In the northern part, the variability of the CO_2 flux is low and the area is covered by relatively cold, saline and low-chlorophyll



NASW. The southern part is highly variable, due to the presence of large mesoscale anticyclonic eddies. In January and February 2020, two NBC rings influence the physical and biogeochemical properties of the region. The NBC retroflection is characterized by waters with equatorial origins that are relatively warm, saline and high in $f\text{CO}_2$. As the rings separate from the retroflection, they interact with the surrounding waters, and the initial signal in $f\text{CO}_2$ is dampened. The main impact of the rings is therefore not necessarily on the surface water they transport in their core, but rather on the filament they stir off the coast. A fresh plume from the Amazon River is transported by the coastal current up to the French Guiana shelf in the beginning of February. The NBC rings entrain the plume of freshwater up to 12°N . This plume is fresh, rich in $\text{Chl}a$ and low in $f\text{CO}_2$ and strongly contrasts with the surrounding waters and spreads over $\sim 100\,000\text{ km}^2$. On the shelf not influenced by the plume water is relatively saline, high in $f\text{CO}_2$ and $\text{Chl}a$, probably due to high concentration of detrital material. As ring A2 propagates westward, it continuously stirs a thin (10 km wide) filament of high $f\text{CO}_2$ shelf water up to 12°N .

Based on the ship observations we identify distinct regime in $f\text{CO}_2$ linked to certain combinations of SST, SSS, and $\text{Chl}a$ properties. We use this information to construct high-resolution maps of $f\text{CO}_2$ and air-sea CO_2 flux using satellite maps of SSS, SST and $\text{Chl}a$. On average over the month of February, the region acts as a strong sink of CO_2 (-1.7 TgC/month), the sink being five times smaller in air-sea CO_2 flux climatologies. The NASW contributes for most of the flux (60%) due to low temperature associated to winter cooling and strong winds. South of Barbados, the region acts also as a sink of CO_2 . The influence of equatorial water is localized to the retroflection region that acts as a small source of CO_2 . The main feature in this part of the domain is the fresh plume that contributes to almost 20% of the total sink.

The processes described here highlight the high variability of air-sea CO_2 fluxes in winter, that are quite different from the ones in summer. These features are relatively common in winter and can be used to better understand the interannual variability of air-sea CO_2 fluxes. The northern part of the domain is driven by the variability in SST, while the southern one is a combination of the interannual variability of temperature, salinity and chlorophyll. It is therefore linked to the year-to-year variability of the NBC rings and the Amazon outflow.

This study is limited by the paucity of data in the region and for this time period. More $f\text{CO}_2$ data closer to the coast would help to better quantify the influence of shelf water on the flux. The signature of the NBC rings has been described for only two rings that had different signatures. In order to reach more robust conclusions on the transport of surface NBC water by the rings, more eddies should be observed. The variability of $f\text{CO}_2$ occurs at large and small scale. Salinity is one of the most valuable predictors of $f\text{CO}_2$ south of 10°N , but the satellite salinity resolution is much lower than the one of temperature and chlorophyll. To have a more accurate prediction of the $f\text{CO}_2$, a high-resolution SSS product would also be very useful.



Appendix A

Due their long time series, the following SST, Chla and SSS products are used to reconstruct $f\text{CO}_2$ maps in winter in the northwestern tropical Atlantic for other years than 2020. Results are shown on Figure A1. They are different than the satellite products used in the main study, that were only available on a short period.

580 The Operational Sea Surface Temperature and Sea Ice Analysis (OSTIA) SST product, distributed by the CMEMS is used here. Daily maps of SST are produced at a resolution of $1/20^\circ$, available from 1981 to present. OSTIA SST uses most SST data available for a day, from both infrared and microwave inferred SST.

Surface Chla from GlobColour dataset derived from ocean color at a $1/24^\circ$ resolution is used. It is a merged product from multiple satellite missions' observations (SeaWiFS, MERIS, MODIS, VIIRS NPP, OLCI-A, VIIRS JPSS-1 and OLCI-B).

585 GlobColour data is developed, validated, and distributed by ACRI-st.

We also use SMOS and SMAP combined weekly SSS generated by the Climate Change Initiative Sea Surface Salinity (CCI + SSS) project (<https://doi.org/10.5285/4ce685bff631459f-b2a30faa699f3fc5>). It provides weekly level-3 SSS data from 2010 to 2019 at a spatial resolution of 50 km, a sampled on a 25 km x 25 km grid, and 1 day, by combining data from the SMOS, Aquarius, and SMAP missions.

590

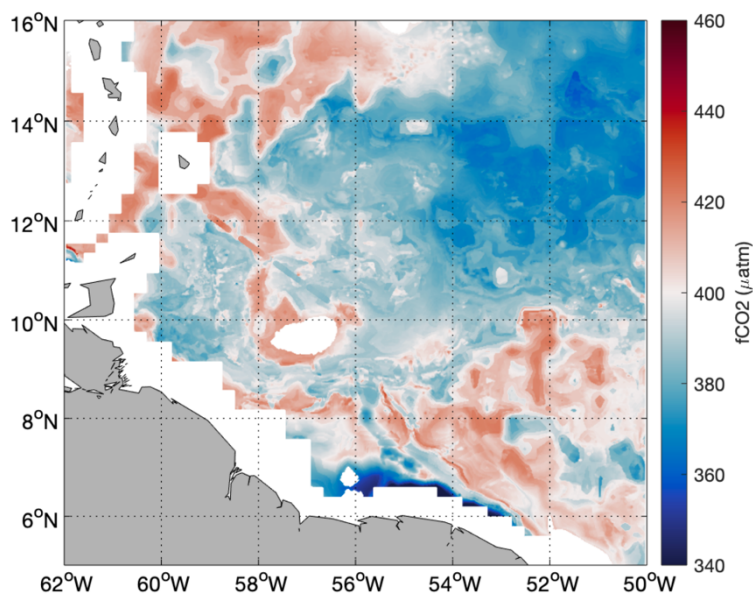


Figure A1. $f\text{CO}_2$ reconstructed from OSTIA SST, CCI+SSS and Globcolour Chla for the 23/12/2015 superimposed with the $f\text{CO}_2$ from cruise 642B20151209.



595

| | Fresh plume | NBC waters | Modified NBC | NASW |
|---|--------------------|-------------------|-----------------------|-------------------------------|
| SOCAT fCO₂ | 316.2 | 413.4 | 385.8 | 349 |
| fCO₂ reconstructed from SOCAT SST & SSS | 310.7 | 410.7 | 392.9 | 358.7 |
| Transect date | 2016/01/05 | 2016/01/08 | 2015/12/23 | 2013/02/10 |
| Ship Name | Colibri (France) | Colibri (France) | MSC Marianna (Panama) | Benguela Stream (Netherlands) |
| Expocode | 35MJ20151229 | 35MJ20160107 | 642B20151209 | 33RO20130108 |

Table A1. Comparison for the 4 main water masses between the fCO₂ from SOCAT transect and the fCO₂ reconstructed from in-situ SSS and SST and colocalized Chl_a.

600 Code Availability

Code used in this study can be made available upon reasonable request to the corresponding author.

Data Availability

We benefited from numerous data sets made freely available and listed here: the ADT produced by Ssalto/Duacs distributed by CMEMS (<https://resources.marine.copernicus.eu>), the Chl_a and SST maps produced by CLS
 605 (<https://datastore.cls.fr/catalogues/chlorophyll-high-resolution-daily> and <https://datastore.cls.fr/catalogues/sea-surface-temperature-infra-red-high-resolution-daily>), the SMOS L2Q field produced by CATDS (CATDS, 2019) (<https://10.12770/12dba510-cd71-4d4f-9fc1-9cc027d128b0>), the SMAP maps produced by Remote Sensing System (RSS v4 40 km), the CCI+SSS maps produced in the frame of ESA CCI+SSS project (<https://10.5285/4ce685bff631459fb2a-30faa699f3fc5>), the OSTIA SST and Copernicus -GlobColour Chl_a distributed by the CMEMS
 610 (SST_GLO_SST_L4_REP_OBSERVATIONS_010_011 and OCEANCOLOUR_GLO_CHL_L4_REP_OBSERVATIONS_009_082).

The RV Atalante fCO₂ is available on the SEANOE website: doi/10.17882/83578. The RV Ron Brown and RV Merian fCO₂ data can be found on the SOCAT database (expocodes 33RO20200106 and 06M220200117 respectively). The Surface Ocean



CO₂ Atlas (SOCAT) is an international effort, endorsed by the International Ocean Carbon Coordination Project (IOCCP), the
615 Surface Ocean Lower Atmosphere Study (SOLAS) and the Integrated Marine Biosphere Research program, to deliver a
uniformly quality-controlled surface ocean CO₂ database. The many researchers and funding agencies responsible for the
collection of data and quality control are thanked for their contributions to SOCAT.

Author contribution

620 LO, JB, GR and NL conceptualized the project. LO carried out the measurements and data analysis. LO, JB, GR, NL and PL
contributed to result interpretation. PL, MR and RW provided the crucial datasets. LO, MR, SS and JK conducted field work.
LO wrote the manuscript with input from all co-authors.

Competing interests

Some authors are members of the editorial board of Biogeosciences. The peer-review process was guided by an independent
625 editor, and the authors have also no other competing interests to declare.

Acknowledgements

This research has been supported by the European Research Council (ERC) advanced grant EUREC⁴A (grant agreement no.
694768) under the European Union's Horizon 2020 research and innovation program (H2020), with additional support from
630 CNES (the French National Centre for Space Studies) through the TOSCA SMOS-Ocean, TOEddies, and EUREC⁴A-OA
proposals, the French national program LEFE INSU, by IFREMER, the French research fleet, the French research
infrastructures AERIS and ODATIS, IPSL, the Chaire Chanel program of the Geosciences Department at ENS and the
EUREC⁴A-OA JPI Ocean & Climate program. LO was supported by a scholarship from ENS and Sorbonne Université. We
thank Jonathan Fin at the Service National d'Analyse des paramètres Océaniques du CO₂ (SNAPO-CO₂) at LOCEAN for the
analysis of DIC and TA samples, and François Baurand at the US IMAGO for the nutrient analysis. We thank Matthieu Labaste
635 and Christophe Noisel for the help with the CO₂ measurements onboard RV Atalante. Kevin Sullivan performed the data
reduction and quality control of data on the Ronald H Brown. We also warmly thank the captain and crew of RVs Atalante,
Maria S. Merian and Ronald H. Brown. The measurements on the Ronald H. Brown were supported by the Global Ocean
Monitoring and Observation (GOMO) program (fund Ref. 100007298).

References

640 Aller, R. C., & Blair, N. E. (2006). Carbon remineralization in the Amazon–Guianas tropical mobile mudbelt: A sedimentary
incinerator. *Continental Shelf Research*, 26(17), 2241–2259. <https://doi.org/10.1016/j.csr.2006.07.016>



- Andrié, C., Oudot, C., Genthon, C., & Merlivat, L. (1986). CO₂ fluxes in the tropical Atlantic during FOCAL cruises. *Journal of Geophysical Research: Oceans*, 91(C10), 11741–11755. <https://doi.org/10.1029/JC091iC10p11741>
- 645 Aroucha, L. C., Veleda, D., Lopes, F. S., Tyaquicã, P., Lefèvre, N., & Araujo, M. (2020). Intra- and Inter-Annual Variability of North Brazil Current Rings Using Angular Momentum Eddy Detection and Tracking Algorithm: Observations From 1993 to 2016. *Journal of Geophysical Research: Oceans*, 125(12), e2019JC015921. <https://doi.org/10.1029/2019JC015921>
- Arrigo, K. R. (2007). Marine manipulations. *Nature*, 450(7169), 491–492. <https://doi.org/10.1038/450491a>
- Arruda, R., Atamanchuk, D., Cronin, M., Steinhoff, T., & Wallace, D. W. R. (2020). At-sea intercomparison of three underway pCO₂ systems. *Limnology and Oceanography: Methods*, 18(2), 63–76. <https://doi.org/10.1002/lom3.10346>
- 650 Bakker, D. C. E., Pfeil, B., Landa, C. S., Metzl, N., O'Brien, K. M., Olsen, A., et al. (2016). A multi-decade record of high-quality *f*CO₂ data in version 3 of the Surface Ocean CO₂ Atlas (SOCAT). *Earth System Science Data*, 8(2), 383–413. <https://doi.org/10.5194/essd-8-383-2016>
- Behrenfeld, M. J., O'Malley, R. T., Siegel, D. A., McClain, C. R., Sarmiento, J. L., Feldman, G. C., et al. (2006). Climate-driven trends in contemporary ocean productivity. *Nature*, 444(7120), 752–755. <https://doi.org/10.1038/nature05317>
- 655 Chen, C.-T. A., Huang, T.-H., Fu, Y.-H., Bai, Y., & He, X. (2012). Strong sources of CO₂ in upper estuaries become sinks of CO₂ in large river plumes. *Current Opinion in Environmental Sustainability*, 4(2), 179–185. <https://doi.org/10.1016/j.cosust.2012.02.003>
- Coles, V. J., Brooks, M. T., Hopkins, J., Stukel, M. R., Yager, P. L., & Hood, R. R. (2013). The pathways and properties of the Amazon River Plume in the tropical North Atlantic Ocean. *Journal of Geophysical Research: Oceans*, 118(12), 6894–6913. <https://doi.org/10.1002/2013JC008981>
- 660 Dai, A., & Trenberth, K. E. (2002). Estimates of Freshwater Discharge from Continents: Latitudinal and Seasonal Variations. *Journal of Hydrometeorology*, 3(6), 660–687. [https://doi.org/10.1175/1525-7541\(2002\)003<0660:EOFDfC>2.0.CO;2](https://doi.org/10.1175/1525-7541(2002)003<0660:EOFDfC>2.0.CO;2)
- Entekhabi, D., Njoku, E. G., O'Neill, P. E., Kellogg, K. H., Crow, W. T., Edelstein, W. N., et al. (2010). The soil moisture active passive (SMAP) mission. *Proceedings of the IEEE*, 98(5), 704–716.
- 665 Fay, A. R., & McKinley, G. A. (2014). Global open-ocean biomes: mean and temporal variability. *Earth System Science Data*, 6(2), 273–284. <https://doi.org/10.5194/essd-6-273-2014>
- Ffield, A. (2005). North Brazil current rings viewed by TRMM Microwave Imager SST and the influence of the Amazon Plume. *Deep Sea Research Part I: Oceanographic Research Papers*, 52(1), 137–160. <https://doi.org/10.1016/j.dsr.2004.05.013>
- 670 Field, C. B., Behrenfeld, M. J., Randerson, J. T., & Falkowski, P. (1998). Primary Production of the Biosphere: Integrating Terrestrial and Oceanic Components. *Science*, 281(5374), 237–240. <https://doi.org/10.1126/science.281.5374.237>
- Font, J., Camps, A., Borges, A., Martín-Neira, M., Boutin, J., Reul, N., et al. (2009). SMOS: The challenging sea surface salinity measurement from space. *Proceedings of the IEEE*, 98(5), 649–665.



- Fournier, S., Chapron, B., Salisbury, J., Vandemark, D., & Reul, N. (2015). Comparison of spaceborne measurements of sea surface salinity and colored detrital matter in the Amazon plume. *Journal of Geophysical Research: Oceans*, 120(5), 3177–3192. <https://doi.org/10.1002/2014JC010109>
- Fratantoni, D. M., & Glickson, D. A. (2002). North Brazil Current Ring Generation and Evolution Observed with SeaWiFS. *Journal of Physical Oceanography*, 32(3), 1058–1074. [https://doi.org/10.1175/1520-0485\(2002\)032<1058:NBCRGA>2.0.CO;2](https://doi.org/10.1175/1520-0485(2002)032<1058:NBCRGA>2.0.CO;2)
- 680 Fratantoni, D. M., & Richardson, P. L. (2006). The Evolution and Demise of North Brazil Current Rings. *Journal of Physical Oceanography*, 36(7), 1241–1264. <https://doi.org/10.1175/JPO2907.1>
- Friedlingstein, P., O’Sullivan, M., Jones, M. W., Andrew, R. M., Hauck, J., Olsen, A., et al. (2020). Global Carbon Budget 2020. *Earth System Science Data*, 12(4), 3269–3340. <https://doi.org/10.5194/essd-12-3269-2020>
- Garraffo, Z. D., Johns, W. E., P.Chassignet, E., & Goni, G. J. (2003). North Brazil Current rings and transport of southern waters in a high resolution numerical simulation of the North Atlantic. In G. J. Goni & P. Malanotte-Rizzoli (Eds.), *Elsevier Oceanography Series* (Vol. 68, pp. 375–409). Elsevier. [https://doi.org/10.1016/S0422-9894\(03\)80155-1](https://doi.org/10.1016/S0422-9894(03)80155-1)
- 685 Grodsky, S. A., Vandemark, D., & Feng, H. (2018). Assessing Coastal SMAP Surface Salinity Accuracy and Its Application to Monitoring Gulf of Maine Circulation Dynamics. *Remote Sensing*, 10(8), 1232. <https://doi.org/10.3390/rs10081232>
- Ibáñez, J. S. P., Araujo, M., & Lefèvre, N. (2016). The overlooked tropical oceanic CO₂ sink. *Geophysical Research Letters*, 43(8), 3804–3812. <https://doi.org/10.1002/2016GL068020>
- 690 IOCCG. (2009). *Partition of the Ocean Into Ecological Provinces: Role of Ocean-colour Radiometry*. Dartmouth Canada.
- IPCC, 2019: IPCC Special Report on the Ocean and Cryosphere in a Changing Climate [H.-O. Pörtner, D.C. Roberts, V. Masson-Delmotte, P. Zhai, M. Tignor, E. Poloczanska, K. Mintenbeck, A. Alegria, M. Nicolai, A. Okem, J. Petzold, B. Rama, N.M. Weyer (eds.)]. In press.
- 695 IPCC, 2021: Climate Change 2021: The Physical Science Basis. Contribution of Working Group I to the Sixth Assessment Report of the Intergovernmental Panel on Climate Change [Masson-Delmotte, V., P. Zhai, A. Pirani, S.L. Connors, C. Péan, S. Berger, N. Caud, Y. Chen, L. Goldfarb, M.I. Gomis, M. Huang, K. Leitzell, E. Lonnoy, J.B.R. Matthews, T.K. Maycock, T. Waterfield, O. Yelekçi, R. Yu, and B. Zhou (eds.)]. Cambridge University Press. In Press.
- Jochumsen, K., Rhein, M., Hüttl-Kabus, S., & Böning, C. W. (2010). On the propagation and decay of North Brazil Current rings. *Journal of Geophysical Research: Oceans*, 115(C10). <https://doi.org/10.1029/2009JC006042>
- 700 Johns, W. E., Lee, T. N., Schott, F. A., Zantopp, R. J., & Evans, R. H. (1990). The North Brazil Current retroflexion: Seasonal structure and eddy variability. *Journal of Geophysical Research: Oceans*, 95(C12), 22103–22120. <https://doi.org/10.1029/JC095iC12p22103>
- Johns, W. E., Zantopp, R. J., & Goni, Gustavo. J. (2003). Cross-gyre transport by North Brazil Current rings. In G. J. Goni & P. Malanotte-Rizzoli (Eds.), *Elsevier Oceanography Series* (Vol. 68, pp. 411–441). Elsevier. [https://doi.org/10.1016/S0422-9894\(03\)80156-3](https://doi.org/10.1016/S0422-9894(03)80156-3)
- 705



- Karstensen, J., Lavik, G., Acquistapace, C., Bagheri, G., Begler, C., Bendinger, A., et al. (2020). *EUREC4A Campaign, Cruise No. MSM89, 17. January - 20. February 2020, Bridgetown (Barbados) - Bridgetown (Barbados), The ocean mesoscale component in the EUREC4A field study* (MARIA S. MERIAN-Berichte) (pp. 1–70). Bonn: Gutachterpanel
710 Forschungsschiffe. https://doi.org/10.2312/cr_msm89
- Kerr, Y. H., Waldteufel, P., Wigneron, J.-P., Delwart, S., Cabot, F., Boutin, J., et al. (2010). The SMOS mission: New tool for monitoring key elements of the global water cycle. *Proceedings of the IEEE*, 98(5), 666–687.
- Körtzinger, A. (2003). A significant CO₂ sink in the tropical Atlantic Ocean associated with the Amazon River plume. *Geophysical Research Letters*, 30(24). <https://doi.org/10.1029/2003GL018841>
- 715 Landschützer, P., Gruber, N., Bakker, D. C. E., Schuster, U., Nakaoka, S., Payne, M. R., et al. (2013). A neural network-based estimate of the seasonal to inter-annual variability of the Atlantic Ocean carbon sink. *Biogeosciences*, 10(11), 7793–7815. <https://doi.org/10.5194/bg-10-7793-2013>
- Landschützer, P., Gruber, N., Bakker, D. C. E., & Schuster, U. (2014). Recent variability of the global ocean carbon sink. *Global Biogeochemical Cycles*, 28(9), 927–949. <https://doi.org/10.1002/2014GB004853>
- 720 Landschützer, Peter, Gruber, N., & Bakker, D. C. E. (2016). Decadal variations and trends of the global ocean carbon sink. *Global Biogeochemical Cycles*, 30(10), 1396–1417. <https://doi.org/10.1002/2015GB005359>
- Landschützer, Peter, Laruelle, G. G., Roobaert, A., & Regnier, P. (2020). A uniform pCO₂ climatology combining open and coastal oceans. *Earth System Science Data*, 12(4), 2537–2553. <https://doi.org/10.5194/essd-12-2537-2020>
- Laxenaire, R., Speich, S., Blanke, B., Chaigneau, A., Pegliasco, C., & Stegner, A. (2018). Anticyclonic Eddies Connecting the
725 Western Boundaries of Indian and Atlantic Oceans. *Journal of Geophysical Research: Oceans*, 123(11), 7651–7677. <https://doi.org/10.1029/2018JC014270>
- Lefèvre, N., Diverrés, D., & Gallois, F. (2010). Origin of CO₂ undersaturation in the western tropical Atlantic. *Tellus B: Chemical and Physical Meteorology*, 62(5), 595–607. <https://doi.org/10.1111/j.1600-0889.2010.00475.x>
- Longhurst, A., Sathyendranath, S., Platt, T., & Caverhill, C. (1995). An estimate of global primary production in the ocean
730 from satellite radiometer data. *Journal of Plankton Research*, 17(6), 1245–1271. <https://doi.org/10.1093/plankt/17.6.1245>
- Longhurst, A. R. (2010). *Ecological Geography of the Sea*. Elsevier.
- Medeiros, P. M., Seidel, M., Ward, N. D., Carpenter, E. J., Gomes, H. R., Niggemann, J., et al. (2015). Fate of the Amazon River dissolved organic matter in the tropical Atlantic Ocean. *Global Biogeochemical Cycles*, 29(5), 677–690. <https://doi.org/10.1002/2015GB005115>
- 735 Mélice, J.-L., & Arnault, S. (2017). Investigation of the Intra-Annual Variability of the North Equatorial Countercurrent/North Brazil Current Eddies and of the Instability Waves of the North Tropical Atlantic Ocean Using Satellite Altimetry and Empirical Mode Decomposition. *Journal of Atmospheric and Oceanic Technology*, 34(10), 2295–2310. <https://doi.org/10.1175/JTECH-D-17-0032.1>



- Mu, L., Gomes, H. do R., Burns, S. M., Goes, J. I., Coles, V. J., Rezende, C. E., et al. (2021). Temporal Variability of Air-Sea
740 CO₂ flux in the Western Tropical North Atlantic Influenced by the Amazon River Plume. *Global Biogeochemical Cycles*,
35(6), e2020GB006798. <https://doi.org/10.1029/2020GB006798>
- Muller-Karger, F. E., McClain, C. R., & Richardson, P. L. (1988). The dispersal of the Amazon's water. *Nature*, 333(6168),
56–59. <https://doi.org/10.1038/333056a0>
- Olivier Léa, Labaste Matthieu, Noisel Christophe, Lefevre Nathalie (2020). Underway fCO₂ distribution during the
745 EUREC4A-OA experiment. SEANOE. <https://doi.org/10.17882/83578>
- Piepmeyer, J. R., Focardi, P., Horgan, K. A., Knuble, J., Ehsan, N., Lucey, J., et al. (2017). SMAP L-band microwave
radiometer: Instrument design and first year on orbit. *IEEE Transactions on Geoscience and Remote Sensing*, 55(4), 1954–
1966.
- Pierrot, D., Neill, C., Sullivan, K., Castle, R., Wanninkhof, R., Lüger, H., et al. (2009). Recommendations for autonomous
750 underway pCO₂ measuring systems and data-reduction routines. *Deep Sea Research Part II: Topical Studies in Oceanography*,
56(8), 512–522. <https://doi.org/10.1016/j.dsr2.2008.12.005>
- Platt, T., Caverhill, C., & Sathyendranath, S. (1991). Basin-scale estimates of oceanic primary production by remote sensing:
The North Atlantic. *Journal of Geophysical Research: Oceans*, 96(C8), 15147–15159. <https://doi.org/10.1029/91JC01118>
- Poisson, A., Metzl, N., Brunet, C., Schauer, B., Bres, B., Ruiz-Pino, D., & Louanchi, F. (1993). Variability of sources and
755 sinks of CO₂ in the western Indian and southern oceans during the year 1991. *Journal of Geophysical Research: Oceans*,
98(C12), 22759–22778. <https://doi.org/10.1029/93JC02501>
- Quinn, P. K., Thompson, E. J., Coffman, D. J., Baidar, S., Bariteau, L., Bates, T. S., et al. (2021). Measurements from the RV
Ronald H. Brown and related platforms as part of the Atlantic Tradewind Ocean-Atmosphere Mesoscale Interaction Campaign
(ATOMIC). *Earth System Science Data*, 13(4), 1759–1790. <https://doi.org/10.5194/essd-13-1759-2021>
- 760 Reverdin, G., Olivier, L., Foltz, G. R., Speich, S., Karstensen, J., Horstmann, J., et al. (2021). Formation and Evolution of a
Freshwater Plume in the Northwestern Tropical Atlantic in February 2020. *Journal of Geophysical Research: Oceans*, 126(4),
e2020JC016981. <https://doi.org/10.1029/2020JC016981>
- Richardson, P. L., Hufford, G. E., Limeburner, R., & Brown, W. S. (1994). North Brazil Current retroflection eddies. *Journal
of Geophysical Research: Oceans*, 99(C3), 5081–5093. <https://doi.org/10.1029/93JC03486>
- 765 Schott, F. A., Fischer, J., & Stramma, L. (1998). Transports and Pathways of the Upper-Layer Circulation in the Western
Tropical Atlantic. *Journal of Physical Oceanography*, 28(10), 1904–1928. [https://doi.org/10.1175/1520-0485\(1998\)028<1904:TAPOTU>2.0.CO;2](https://doi.org/10.1175/1520-0485(1998)028<1904:TAPOTU>2.0.CO;2)
- Speich Sabrina, The Embarked Science Team (2021). EUREC4A-OA. Cruise Report. 19 January – 19 February 2020. Vessel
: L'ATALANTE. <https://doi.org/10.13155/80129>
- 770 Stevens, B., Bony, S., Farrell, D., Ament, F., Blyth, A., Fairall, C., et al. (2021). EUREC⁴A. *Earth System Science Data*, 13(8),
4067–4119. <https://doi.org/10.5194/essd-13-4067-2021>



- Stum, J., Tebri, H., Lehodey, P., Senina, I., Greiner, E., & Lucas, M. (n.d.). NRT operational chlorophyll maps calculation for marine applications, 1.
- 775 Subramaniam, A., Yager, P. L., Carpenter, E. J., Mahaffey, C., Björkman, K., Cooley, S., et al. (2008). Amazon River enhances diazotrophy and carbon sequestration in the tropical North Atlantic Ocean. *Proceedings of the National Academy of Sciences*, 105(30), 10460–10465. <https://doi.org/10.1073/pnas.0710279105>
- Takahashi, T., Sutherland, S. C., Sweeney, C., Poisson, A., Metzl, N., Tilbrook, B., et al. (2002). Global sea–air CO₂ flux based on climatological surface ocean pCO₂, and seasonal biological and temperature effects. *Deep Sea Research Part II: Topical Studies in Oceanography*, 49(9), 1601–1622. [https://doi.org/10.1016/S0967-0645\(02\)00003-6](https://doi.org/10.1016/S0967-0645(02)00003-6)
- 780 Takahashi, T., Sutherland, S. C., Wanninkhof, R., Sweeney, C., Feely, R. A., Chipman, D. W., et al. (2009). Climatological mean and decadal change in surface ocean pCO₂, and net sea–air CO₂ flux over the global oceans. *Deep Sea Research Part II: Topical Studies in Oceanography*, 56(8), 554–577. <https://doi.org/10.1016/j.dsr2.2008.12.009>
- Wanninkhof, R., Lewis, E., Feely, R. A., & Millero, F. J. (1999). The optimal carbonate dissociation constants for determining surface water pCO₂ from alkalinity and total inorganic carbon. *Marine Chemistry*, 65(3), 291–301.
- 785 [https://doi.org/10.1016/S0304-4203\(99\)00021-3](https://doi.org/10.1016/S0304-4203(99)00021-3)
- Wanninkhof, R. (2014). Relationship between wind speed and gas exchange over the ocean revisited. *Limnology and Oceanography: Methods*, 12(6), 351–362. <https://doi.org/10.4319/lom.2014.12.351>
- Weiss, R. F. (1974). Carbon dioxide in water and seawater: the solubility of a non-ideal gas. *Marine Chemistry*, 2(3), 203–215. [https://doi.org/10.1016/0304-4203\(74\)90015-2](https://doi.org/10.1016/0304-4203(74)90015-2)
- 790 Wilson, W. D., Johns, W. E., & Garzoli, S. L. (2002). Velocity structure of North Brazil Current rings. *Geophysical Research Letters*, 29(8), 114-1-114–4. <https://doi.org/10.1029/2001GL013869>